Heliyon 10 (2024) e35387

Contents lists available at ScienceDirect

Heliyon

journal homepage: www.cell.com/heliyon

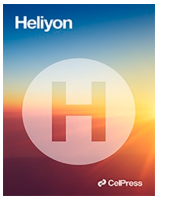

Research article

Optimization and analysis of battery thermal management system structure based on flat heat pipes and biomimetic fins

Zeyu Liu [a,b], Chengfeng Xiong [a,b], Xiaofang Du [a,b,*]

[a] College of Automotive Engineering, Wuhan University of Technology, Wuhan, 430070, China
[b] Hubei Key Laboratory of Advanced Technology for Automotive Components, Wuhan University of Technology, Wuhan 430070, China

ARTICLE INFO

Keywords:
Lithium-ion batteries
Flat heat pipe
Heat dissipation fins
Orthogonal experiment
Fuzzy grey relational analysis

ABSTRACT

As one of the key components of electric vehicles, the enhancement of the performance of the power battery is closely intertwined with an efficient Battery Thermal Management System (BTMS). In the realm of BTMS, Flat Heat Pipes (FHP) have garnered considerable attention due to their lightweight structure and excellent thermal conductivity. Thus, a BTMS configuration scheme based on FHP is proposed in this study. Utilizing orthogonal design and fuzzy grey relational analysis as the evaluation methods, coupled with numerical simulations, an investigation into the influence of four structural parameters of the novel biomimetic fins (namely, the diameter, height, spacing of protrusions, and height of cooling fins) on the temperature distribution of the battery pack is conducted. The research findings indicate that to maintain the battery within an optimal operational temperature range, the optimal dimensional parameters should be controlled at 17.5 mm, 4 mm, 13 mm, and 90 mm, respectively. Subsequent sensitivity analysis reveals that the height of the protrusions exhibits the most significant influence on the maximum temperature of the module, whereas the height of the cooling fins exerts a considerable impact on the consistency of the module temperature. The optimized maximum temperature is determined to be 36.52 °C, with a temperature difference of 2.65 °C.

Nomenclature

D	Fish scale length(mm)
H	Fish scale height(mm)
S	Fish scale interval(mm)
c	Specific Heat Capacity(J/kg·K)
t	Time step(s)
T	Temperature(K)
q	Heat generation rate(W/m^3)
R	Internal resistance(Ω)
I	Charging current(A)
Q_{in}	Heat input(J)
R_{ov}	Thermal resistance of heat pipe(K/W)
H	Enthalpy(J)
p	Static pressure(Pa)
Greek letters	

(*continued on next page*)

* Corresponding author. College of Automotive Engineering, Wuhan University of Technology, Wuhan, 430070, China.
E-mail address: 286411@whut.edu.cn (X. Du).

https://doi.org/10.1016/j.heliyon.2024.e35387
Received 19 May 2024; Received in revised form 17 July 2024; Accepted 27 July 2024
Available online 3 August 2024

(*continued*)

ρ	Density(kg/m^3)
λ	Thermal conductivity(W/(m·K))
α	Mass fraction(%)
μ	Dynamic viscosity(Pa·s)
v	Vapor
Subscripts and superscripts	
b	battery
v	volume
e	evaporation
cl	condensation
l	liquid
E	energy
a	air
Acronyms	
BTMS	Battery Thermal Management System
FHP	Flat Heat Pipes
PCM	Phase Change Materials
CFD	Computational Fluid Dynamics
LCP	Liquid cooling plates
GRA	Grey Relation Analysis
OCV	Open Circuit Voltage
DOD	Depth of Discharge

1. Introduction

With continuous progress in both economy and technology, issues such as energy shortages, climate warming, and environmental pollution are increasingly severe [1]. Measures are being taken by countries worldwide to promote the use of clean energy to replace the combustion of fossil fuels [2,3]. Electric vehicles, as environmentally friendly transportation products, have received widespread attention. Lithium-ion batteries, due to their high energy density and long cycle life, have become the most widely used type of power battery [4–6]. However, the performance of lithium-ion batteries is closely related to their operating temperature [7]. In electric vehicles, where batteries are numerous and densely packed, the heat generated during operation is difficult to dissipate rapidly and uniformly. This not only leads to elevated battery operating temperatures and significant temperature differentials but also increases the risk of thermal runaway and capacity degradation due to improper thermal management [8]. For lithium-ion battery packs, the optimal operating temperature ranges from 25 °C to 40 °C, with a temperature differential of less than 5 °C [9]. Consequently, configuring an appropriate battery thermal management system is crucial for maintaining optimal battery performance and preventing thermal instability and capacity loss [10].

The classification of Battery Thermal Management Systems (BTMS) is based on their cooling techniques, which can be categorized into two main types: active cooling and passive cooling [11]. Active cooling techniques primarily encompass methods such as air cooling, liquid cooling, and immersion cooling, while passive cooling techniques include the utilization of heat pipes, Phase Change Materials (PCMs), and natural convection for heat regulation [12]. Koorata et al. [13] explores a diagonal minichannel thermal management system for a 20 Ah pouch cell, showing how optimal cooling strategies, including a specific inlet temperature and flow rate, enhance temperature uniformity and reduce pressure drops. A comparative analysis confirms a 75 % improvement in temperature homogeneity, with the system keeping peak temperatures 20 % below the safety threshold for Li-ion cells. Pu et al. [14] optimizes a serpentine-channel cold plate (SCP) for lithium-ion battery thermal management, using a novel variable cross-section design (VCDSCP). The VCDSCP significantly improves thermal management by reducing temperature peaks and disparities, enhancing performance at high discharge rates with reduced pressure drop. Additionally, hybrid cooling systems combining both active and passive cooling techniques are widely prevalent in modern battery thermal management [15]. From an efficiency perspective, active cooling methods demonstrate superior performance in controlling battery temperature. For instance, liquid cooling systems, owing to their high heat capacity and excellent thermal conductivity, exhibit outstanding performance in handling high-power output applications. This advantage makes them more favorable in long-distance driving and high-power demand electric vehicles [16]. However, the design and implementation of liquid cooling systems are relatively complex, involving additional components such as pipelines, pumps, and heat exchangers, thereby increasing manufacturing and maintenance costs and posing a risk of leakage.While air cooling offers a simple structure, it faces challenges in meeting the high heat dissipation requirements of electric vehicles [17]. Phase Change Materials (PCMs) and heat pipes are typically employed as heat transfer media in passive cooling systems. PCMs have lower thermal conductivity and are more challenging to encapsulate, limiting their application. Talele et al. [18] explore innovative solutions to thermal management challenges in lithium-ion batteries by employing graphene-enhanced composite phase change materials (CPCM). By incorporating a layer of CPCM, the study seeks to delay the onset of thermal runaway, thereby enhancing safety through the provision of early warning alerts for elevated temperatures. Hossein et al. [19] study investigated the impact of heated wall shapes on PCM melting within a rectangular cavity. The curvy wall configuration significantly enhanced the melting process, reducing time by 57.6 % and increasing energy storage by 16.3 %. Heat pipes, on the other hand, possess excellent heat transfer performance and temperature uniformity due to their extremely high thermal conductivity. However, constrained by limited heat transfer surface area, heat pipes are usually used in conjunction with other cooling elements or strategies to achieve better cooling performance [20]. Typically, fins are used to enhance the cooling performance of heat pipe-based battery thermal management systems.Zheng et al. [21]

designed a thermal management system based on finned heat pipes, which reduced the temperature of a battery discharged at 1 C (Represents the ratio of the speed of charging or discharging to its nominal capacity.) to 35.6 °C. When the spacing between fins was 3 mm, the battery achieved optimal temperature uniformity. Wang et al. [22] proposed a BTMS configuration scheme based on flat heat pipes, establishing a coupled model of heat pipes and batteries by considering the vapor flow effect of the working medium in the heat pipes. Experimental results showed that this model could limit the highest temperature to below 50 °C. Ren et al. [23] introduces a top liquid-cooling thermal management system (TLC TMS) using a Z-shaped micro heat pipe array as the core heat transfer element, compared to the traditional bottom liquid-cooling system. Results indicate that the TLC TMS significantly outperforms the bottom system in managing thermal conditions at a 3C charge-discharge rate, effectively reducing temperature rise and variance across the battery module. Due to its flexibility in manufacturing and long lifespan, heat pipe cooling still holds significant potential in battery thermal management. However, research on heat pipe-based BTMS primarily focuses on simple combinations with other cooling methods, lacking further optimization of the structure and specific analysis of multiple factors.

In addition to cooling strategies, enhancing the performance of battery management systems is also of paramount importance. Researchers have been searching for factors influencing BTMS to obtain the optimal cooling method. Experimental testing and numerical simulations are utilized to analyze the temperature distribution of battery packs. A variable heat transfer pathway BTMS was developed by Wu et al. [24] using numerical algorithms combined with Computational Fluid Dynamics (CFD), optimizing parameters of the slots in the structure, thereby reducing temperature differences on the battery surface but slightly increasing the maximum temperature of the battery. Chen et al. [25] proposed a novel hybrid BTMS, incorporating PCM and embedded liquid cooling structure, utilizing response surface methodology to optimize structural parameters. The results indicated that at a flow rate of 0.09 g/s, the liquid proportion of PCM decreased from 57 % to 26 %. Xie et al. [26] conducted extensive research on the shape and macrostructure design of liquid cooling plates (LCP), analyzing the relationship between the internal structure of LCP and temperature control performance. The results demonstrated that increasing the number of diverters within a certain range effectively reduces temperature and temperature differentials. However, the aforementioned studies still have limitations in controlling battery temperature distribution, failing to adequately balance temperature differentials and high temperatures within the system, with room for further optimization in structure.

In industrial manufacturing, inspiration from the wisdom of nature's organisms is often drawn upon to develop relevant biomimetic structures. Inspired by bionic principles and based on the Tesla valve's design, Zhang et al. [27] introduced an innovative bionic blade-like mini-channel liquid cooling plate. An initial thermal simulation model for this cooling plate was developed under 5C discharge conditions using Computational Fluid Dynamics (CFD) methods. The model's reliability was subsequently confirmed through empirical testing. It was found that the channel height exerted the most substantial influence on both the average temperature and the friction coefficient. Moreover, a strong correlation was observed between the internal angle and the heat transfer coefficient. Xu et al. [28], inspired by the unique 3D wavy microstructure of grapefruit peel vascular bundles, proposed a honeycomb structure with wavy features to develop a novel energy-absorbing structure with ideal energy absorption performance. Experimental results indicate that the layered honeycomb design helps reduce initial peak forces, thus preventing excessive peak collision forces from causing harm to personnel or equipment. Xiong et al. [29] designed a heat exchanger with a biomimetic flow channel structure and applied it to cylindrical lithium battery modules. Experiments showed that the highest temperature, maximum temperature difference, and pressure drop of the heat exchanger BTMS under optimal parameters were calculated as 302.656 K, 3.726 K, and 29.69 Pa, respectively. These biomimetic designs can yield significant thermal performance optimizations while considering the feasibility of actual industrial manufacturing applications. However, due to the complexity of their structural processing, they often encounter challenges in practical implementation.

In this paper, a novel thermal management structure based on flat heat pipes and biomimetic fins is designed, employing a thermal pad to enhance the heat conduction between the battery and the heat pipe. Numerical models of the heat pipe and battery module are

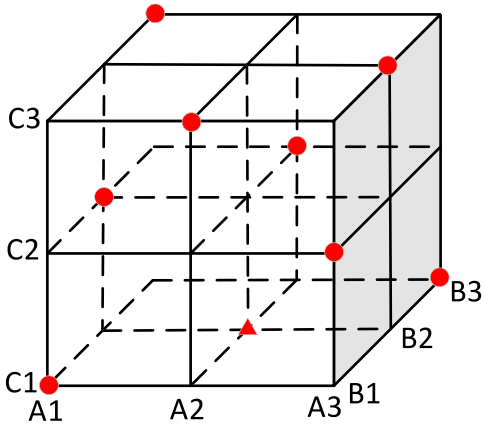

Fig. 1. Orthogonal experiment diagram.

established, and their effectiveness is comprehensively validated through experiments. Simulations based on orthogonal design are conducted to analyze the impact of four factors of the fins on the temperature distribution of the battery system. Fuzzy correlation analysis is employed to evaluate the relationship between the factors and the temperature of the battery pack. Optimal combinations of the main influencing factors and parameters are obtained. Moreover, given that most studies on heat pipes currently adopt simplified thermal resistance models due to the complexity of their operational processes, this paper focuses on considering the phase-change process within the heat pipe. The aim of this research is to provide theoretical guidance for the optimized design of battery thermal management systems based on heat pipes and fins.

2. Evaluation method

2.1. Orthogonal design

When it comes to the impact of multiple factors on the system, conducting sensitivity analysis efficiently is a crucial issue. Orthogonal experiments are a method based on probability theory and mathematical statistics, utilized to obtain comprehensive data by selecting a small number of representative experimental conditions when considering multiple factors [30]. The core concept of this method is to design an experimental matrix, ensuring that the combinations of factor levels appear with equal frequency in the experiments, thereby enabling the experimental results to better represent the overall situation.The orthogonal experimental model is shown in Fig. 1.

In this study, the impact of four structural parameters on the maximum temperature and temperature difference of the battery pack was investigated using orthogonal experimental methods. A Latin square experimental design containing four factors and four levels, namely L16 (44), was employed.

2.2. Fuzzy grey relational analysis

In 2008, The Grey Relational Analysis (GRA), a multi-attribute decision-making (MADM) method, has been proposed for selecting the best option from multiple available alternatives [31]. GRA is primarily aimed at addressing relationships among objects with few samples, lacking experience in problem handling, and unclear potential relationships. GRA offers significant analytical advantages and is also extremely convenient [32].

Grey relational analysis belongs to the theory of grey systems and has been proven to be applicable for handling problems with insufficient information and uncertainty, significantly reducing losses caused by asymmetric information. Simultaneously, grey relational analysis helps to mitigate the shortcomings of statistical regression, suitable for resolving complex interrelationships among multiple factors and variables. It requires less data and demonstrates distinct advantages in addressing multi-objective optimization problems. Building upon this foundation, fuzzy membership degree and Euclidean grey correlation are utilized to enhance this method, thereby assessing the influence of various factors. The specific steps are as follows.

Step 1. Reference and comparison sequences are selected. The reference sequence reflects the data sequence of the behavioral characteristics of the system under study. The changing pattern of each data group can be regarded as the actual variation of a certain behavioral characteristic of the system, as illustrated by Equation (1).

$$Y_T = [y_t(1)\ \ y_t(2)\ \ y_t(3) \cdots y_t(n)] \tag{1}$$

The comparison sequence reflects the data sequence composed of factors influencing the behavior of the system under study. Assuming there are m factors affecting the system under study, and each factor has n operating conditions, the corresponding comparison sequence matrix is shown in Equation (2).

$$X_T = \begin{bmatrix} X_1(k) \\ X_2(k) \\ X_3(k) \\ \vdots \\ X_m(k) \end{bmatrix} = \begin{bmatrix} x_1(1) & x_1(2) & x_1(3) & \cdots & x_1(n) \\ x_2(1) & x_2(2) & x_2(3) & \cdots & x_2(n) \\ x_3(1) & x_3(2) & x_3(3) & \cdots & x_3(n) \\ \vdots & \vdots & \vdots & \vdots & \vdots \\ x_m(1) & x_m(2) & x_m(3) & \cdots & x_m(n) \end{bmatrix} \tag{2}$$

Step 2. Non-dimensionalization of the original data is performed. When applying grey relational analysis, it is essential to non-dimensionalize the original data because each value may have different physical meanings and numerical units, making direct comparative analysis of values impossible. Therefore, non-dimensionalization of the original values is indispensable. The non-dimensionalization of relevant parameter data is based on the method of data range normalization.

$$X_j = [x_j(1)\ \ x_j(2)\ \ x_j(3) \cdots x_j(n)] \tag{3}$$

$$x_j'(k) = \frac{x_j(k) - \min\limits_{1\le k\le n} x_j(k)}{\max\limits_{1\le k\le n} x_j(k) - \min\limits_{1\le k\le n} x_j(k)} \tag{4}$$

In the equation, j represents the number of different influencing factors, with $j = 1,2,3$; k represents the different operating conditions of the influencing factors, with $k = 1,2,3,\cdots,n$.

Step 3. Fuzzy membership degree calculation is performed. The cosine angle method is utilized, which is unaffected by the linear proportional relationship of the data. The similarity between the reference sequence and the comparison sequence can be assessed by the cosine value of the angle between the parameters. The expression is as follows:

$$r_1 = \frac{\sum\limits_{k=1}^{n} y_t(k)x_j(k)}{\sqrt{\sum\limits_{k=1}^{n} y_t^2(k)}\sqrt{\sum\limits_{k=1}^{n} x_j^2(k)}} \tag{5}$$

In the equation, $y_t(k)$ and $x_j(k)$ represent the corresponding values of the reference sequence and the comparison sequence under the k-th operating condition.

Step 4. The degree of correlation refers to the extent of difference in the geometric shapes of the corresponding curves of the target objects under study. The closer the curves are, the greater the correlation between the corresponding sequences; conversely, the farther they are, the smaller the correlation. In general, a reference sequence may correspond to multiple comparison sequences. The correlation coefficient between these two types of sequences under different operating conditions can be expressed as Equation (6). The grey correlation coefficient reflects the degree of correlation between them under different operating conditions.

$$\xi_{ij}(k) = \frac{\min\limits_{1\le j\le m}\min\limits_{1\le j\le n}\left|y_t(k) - x_j(k)\right| + \rho\max\limits_{1\le j\le m}\max\limits_{1\le j\le n}\left|y_t(k) - x_j(k)\right|}{\left|y_t(k) - x_j(k)\right| + \rho\max\limits_{1\le j\le m}\max\limits_{1\le j\le n}\left|y_t(k) - x_j(k)\right|} \tag{6}$$

In the equation, ρ is the resolution coefficient, which is an important factor directly influencing the resolution of the entire system's correlation analysis. Its value is inversely proportional to the resolution and is an empirical constant independent of Y_T and X_T. Its calculation formula is as follows:

$$b = \frac{\frac{1}{m\bullet n}\sum\limits_{j=1}^{m}\sum\limits_{k=1}^{n}\left|y_t(k) - x_j(k)\right|}{\max\limits_{1\le j\le m}\max\limits_{1\le j\le n}\left|y_t(k) - x_j(k)\right|} \tag{7}$$

$$\rho = \begin{cases} 1.25b, b < 1/3 \\ 1.75b, b \ge 1/3 \end{cases} \tag{8}$$

Step 5. : The calculation of Euclidean grey correlation degree is conducted. To enhance the accuracy of the evaluation method, the Euclidean distance from fuzzy mathematics is adopted to assess the differences between the reference array and the comparison array. Specifically, the calculation steps of the Euclidean grey correlation degree (r_2) are as follows:

$$r_2 = 1 - \frac{1}{\sqrt{n}}\sqrt{\sum_{k=1}^{n}\left[1 - \xi_{ij}(k)\right]^2} \tag{9}$$

Step 6. The calculation of fuzzy grey correlation degree is conducted. The calculation of fuzzy grey correlation degree depends on the level of fuzzy membership degree and the value of Euclidean grey correlation degree r.

$$r = \sqrt{\frac{r_1^2 + r_1^2}{2}} \tag{10}$$

Step 7. The evaluation and analysis of the correlation degree of the investigated factors are conducted. By ranking the fuzzy grey correlation degrees, the degree of correlation between factors can be determined, and the closer the correlation is to 1, the stronger the correlation of this factor is indicated.

3. Model description

3.1. Geometry model description

In electric vehicles, the battery thermal management system is typically comprised of battery modules, cooling channels, and heat conducting media. In this study, the L148N50 ternary lithium-ion battery was used as the power source, as shown in Table 1 for the technical parameters. Flat heat pipes and heat dissipation fins were utilized as the heat conduction components, with forced air cooling provided by fans. The designed thermal management system structure is illustrated in Fig. 2. The structure consists of 12 battery modules arranged in parallel, with aluminum plates placed between the batteries. This arrangement can improve the heat dissipation performance, temperature uniformity, and structural stability of the battery modules, thus enhancing the safety and reliability of the battery system. Flat heat pipes are positioned below the battery modules, with the structure depicted in Fig. 3.

The heat pipes consist of a shell, a liquid core, and internal working fluid. The designed dimensions are 446 × 148 × 5 mm. Thermal grease is applied between them to reduce the contact thermal resistance and ensure efficient heat transfer. Above the condensation section of the heat pipes, 24 fins with a thickness of 1 mm are arranged in a staggered pattern for air cooling. The surface of the fins is designed with a streamlined biomimetic structure to increase surface area and enhance convective heat transfer. The raised small blocks disturb the boundary layer, increasing its thickness and improving heat transfer efficiency, while the streamlined biomimetic structure prevents the formation of adverse pressure gradients, reducing system energy consumption. During operation, the heat generated by the battery modules is transferred to the evaporation section of the heat pipe via a thermal pad, where it evaporates into vapor. Subsequently, the vapor flows to the condensation section due to the pressure difference and enters the fins, finally being carried away by air cooling. The dimensions of the thermal management structure have a certain influence on the heat dissipation of the battery modules. This study investigates the effects of four structural factors, namely biomimetic structure parameters D, H, S, and the height of the heat dissipation fins L, on the maximum temperature and temperature uniformity of the battery modules.

3.2. Geometry model description

Utilizing numerical simulation for battery thermal simulation offers cost-effectiveness, flexibility, good safety, and abundant data acquisition, enabling the analysis of sensitivity factors affecting the temperature distribution of battery packs. In this study, three-dimensional models were constructed using CATIA software. Subsequently, simulation tasks were performed using ANSYS Fluent 2022R2 software, supplemented by Fluent Meshing for effective grid partitioning. Fig. 7 illustrates the computational domain for the battery thermal management system model employing Flat Heat Pipes (FHP), with the unstructured grid of the solution domain segmented using Fluent Meshing. In regions containing thin fins, the surface mesh is densified, and three boundary layers are established in the forced convection areas, each layer approximately half the size of the initial grid at the contact boundary. Generally, surface mesh distortion should remain below 0.7 and volume mesh distortion below 0.9 to be deemed acceptable. If certain meshes

Table 1
Lithium battery technical parameters.

Type	Parameter Specifications
Dimensions	148.3mm × 26.7mm × 98 mm
Positive Electrode Material	NCM
Electrolyte	LiPF6
Negative Electrode Material	Graphite
Norminal Capacity	50Ah
Rated Voltage	3.65V
Battery Weight	895g
Operating Voltage Range	2.75V–4.25V
Max Charging Current	300A(instantaneous), 60A(continuous)
Max Discharge Current	400A(instantaneous), 50A(continuous)

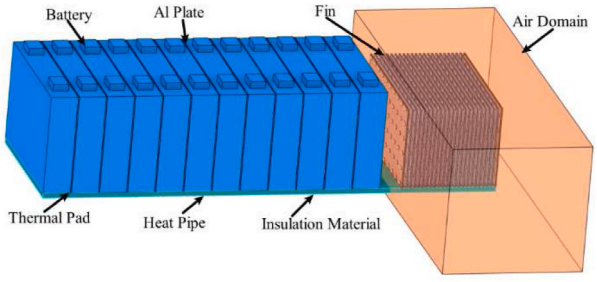

Fig. 2. The thermal management system structure.

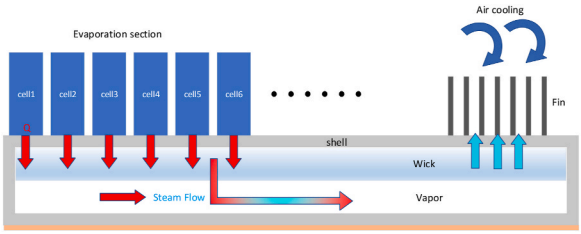

Fig. 3. The structure of flat heat pipes.

Table 2
Physical parameters of acetone [33].

Name	Density (kg/m^3)	Specific Heat Capacity (J/kg·K)	Thermal Conductivity (W/m·K)	Viscosity (Kg/m·s)	Latent Heat Vaporization (KJ/kg)
Acetone(Gas)	0.5542	1452.37	0.0261	7.25×10^{-6}	523
Acetone (Liquid)	791	2160	0.18	3.31×10^{-6}	

Table 3
Thermal Properties Table [34].

Name	Density(kg/m^3)	Specific Heat Capacity(J/kg·K)	Thermal Conductivity(W/m·K)
Battery	2249	1022.8	13/8/9
Heat Pipe	1359.5	1271	220.4/1200.8/220.4
Aluminum	2719	871	202.4
Copper	8978	387.6	381
Air	1.225	1005	0.0262

exhibit inferior quality, optimization is imperative; surface meshes are refined using the Diagnostic Tool, and volume meshes through Auto Node Move. The resulting mesh configuration consists of 334,565 elements with a maximum skewness of 0.37. A y + value of 1 suggests that the non-dimensional distance from the wall to the first layer of nodes is optimally chosen for this model, enabling a reliable simulation of the turbulence characteristics in the vicinity of the wall. Hexahedral meshes are employed throughout the areas including the battery pack module, FHP, and cooling fins. Acetone (parameters listed in Table 2) was utilized as the working fluid for the heat pipe due to its high thermal conductivity, low surface tension, low viscosity, high latent heat of evaporation, wide temperature range, and ease of availability, making it suitable for applications requiring efficient heat transfer. The physical properties of the materials used in the numerical model are detailed in Table 3.

3.2.1. Battery model

In this paper, the positive and negative electrodes of lithium batteries are not considered, and it is assumed that various materials inside the battery exhibit isotropy and uniform distribution. Their specific heat capacity, density, and thermal conductivity are assumed to remain constant with temperature variations. The heat generation within the battery is assumed to be uniform [35]. Therefore, the heat conduction differential equation for the battery in Cartesian coordinates is expressed as follows:

$$\rho_b c_b \frac{\partial T_b}{\partial t} = \lambda_x \frac{\partial^2 T_b}{\partial x^2} + \lambda_y \frac{\partial^2 T_b}{\partial y^2} + \lambda_z \frac{\partial^2 T_b}{\partial z^2} + q_v \tag{11}$$

In the equation, ρ_b, c_b, q_v, and T_b represent the density (kg/m^3), specific heat capacity (J/(kg·K)), volumetric heat generation rate (W/m^3), and temperature (K) of the battery, respectively; λ_x, λ_y, and λ_z denote the thermal conductivity (W/(m·K)) of the lithium battery in the x, y, and z directions, respectively. The variable t stands for time (s).The value of q_v in the equation above is obtained from the battery heat generation equation delineated in Ref. [36].

$$q_v = \frac{1}{V_b}\left(I^2 R - I T_b \frac{\partial U_{OCV}}{\partial T_b}\right) \tag{12}$$

In the equation, V_b represents the volume of the battery (m^3); I denotes the charging current (A); $\frac{\partial U_{OCV}}{\partial T_b}$ represents the temperature entropy coefficient of the battery, which ranges from 1 to 2.8×10^{-4}V/K; R stands for the internal resistance of the battery (Ω). The electrical characteristics and thermal property parameters of the battery are obtained from Ref. [37].

To obtain the internal resistance of the cell, used to verify the accuracy of the battery heat generation model. The internal resistance of the battery was tested using the Hybrid Pulse Power Characterization (HPPC) method. The total internal resistance of the battery can be obtained by adding the ohmic resistance and the polarization resistance, as shown in the following formula:

$$R_{total} = R_{\Omega} + R_p = \frac{U_1 - U_2}{I} + \frac{U_2 - U_3}{I}$$

where U_1 is the battery voltage before applying the pulse current (V), U_2 is the battery voltage at the moment the pulse current is applied, U_3 is the battery voltage after the pulse current has been applied for a period of time, and I is the applied pulse current (A).

Fig. 4 shows the experimental results of HPPC tests under different ambient temperatures and discharge rates. By analyzing the graphs, the following conclusions can be drawn.

(1) At the same ambient temperature, when SOC $\geq$0.3, the total internal resistance of the battery changes little; when SOC $<$0.3, the internal resistance increases significantly. The pulse current rate has a large impact on the internal resistance.
(2) At the same pulse current rate, an increase in temperature reduces the battery's internal resistance, especially at low states of charge.
(3) Under constant pulse current rate and ambient temperature, the internal resistance of the battery is stable when SOC $\geq$0.3; when SOC $<$0.3, the internal resistance changes dramatically due to polarization reactions causing an increase in internal resistance.

3.2.2. Heat pipe model

The flat heat pipe utilizes the principle of heat absorption through phase change of the working fluid, characterized by a high heat transfer coefficient, high temperature uniformity, and variable heat flow direction.The thermal resistance R of the flat heat pipe can be determined by Fourier's law of heat conduction, as follows:

$$R = \frac{\Delta T}{Q} \tag{13}$$

The overall thermal resistance R_{ov} of the flat heat pipe can be defined as the ratio of the temperature difference between the average temperatures of the evaporator section T_e and the condenser section T_{cl} to the input heat flux under steady-state operation.

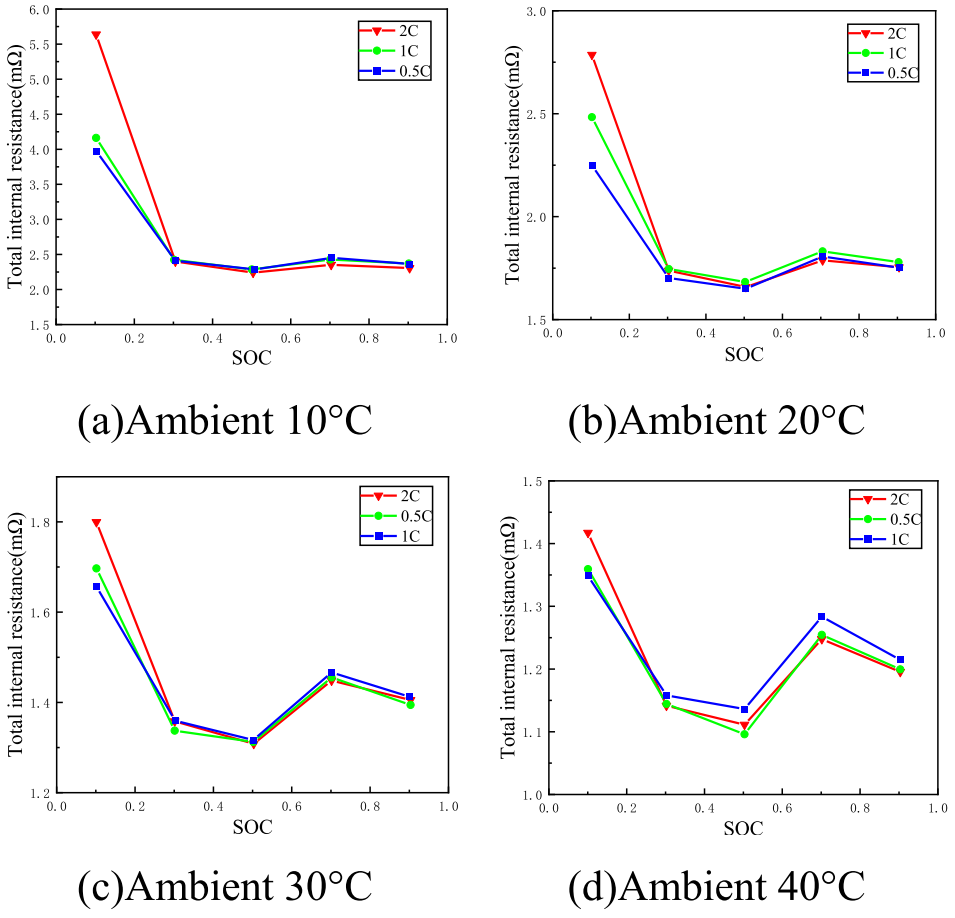

Fig. 4. Total internal resistance of lithium battery experiment (a)Ambient 10 °C (b)Ambient 20 °C (c)Ambient 30 °C (d)Ambient 40 °C.

$$R_{ov} = \frac{T_e - T_{cl}}{Q_{in}} \tag{14}$$

The equivalent heat transfer coefficient of the heat pipe is calculated using the following formula:

$$K_{eff} = \frac{Q \bullet L_{eff}}{(T_e - T_{cl}) \bullet A_c}$$

where K_{eff} is the equivalent heat transfer coefficient (W/m·K); A_c is the cross-sectional area of the heat pipe (m^2); L_{eff} is the effective length of the heat pipe (m), calculated using the following formula:

$$L_{eff} = \frac{L_e + L_c}{2} + L_a$$

where L_e is the length of the evaporator section (m); L_c is the length of the condenser section (m); L_a is the length of the adiabatic section (m).

Figs. 5 and 6 show the relationships between the equivalent thermal resistance and the equivalent heat transfer coefficient of the designed micro-grooved flat heat pipe with the heat source power, respectively. The equivalent thermal resistance of the heat pipe decreases with the increase of the heat source power, while the equivalent heat transfer coefficient increases. The reason is that as the heat source power increases, the phase change process of the working fluid inside the heat pipe becomes more intense, thus enhancing the heat transfer performance of the heat pipe. The thermal conductivity or thermal resistance of the heat pipe changes with temperature or heat source variations, which is achieved in the simulation through interpolation of the above formulas and simulation results.

During the simulation, the volumetric heat source simulation results of each battery were extracted, and the flat heat pipe was simplified as a conductor. The thermal conductivity in the length direction was calculated by interpolating the total heat generation power of the battery, while the thermal conductivity in other directions adopted the thermal conductivity of the shell material. The steady-state fluid-solid coupling simulation used the SIMPLE algorithm and First Order Upwind discretization scheme, with a convergence precision set to 10^{-5}.

From the current perspective of heat pipe research, due to the complexity of heat pipe operation, the model research on heat pipe heat transfer performance mainly adopts simplified heat pipe models, which simplifies the heat pipe to a thermal resistance and verifies the results through relevant heat pipe experiments, most of which do not study heat transfer from the phase change process of the heat pipe itself. Therefore, in this paper, emphasis will be placed on considering the phase change process inside the heat pipe and establishing an overall thermal resistance equivalent model of the heat pipe through numerical simulation methods.

When conducting phase-change heat simulation of the heat pipe using Fluent software, the simulation of the internal phase-change process of the heat pipe is achieved by modifying the control equation source terms through the creation of UDFs. These source terms encompass energy source terms for the conversion between gas and liquid phases and mass source terms for the mutual conversion between gas and liquid phases. The expressions for each source term are provided below.

(1) Mass source term: When the evaporation temperature $T_l > T_{sat}$ for the liquid phase:

$$S_M = -0.1\alpha_l\rho_l\left|\frac{T_l - T_{sat}}{T_{sat}}\right| \tag{15}$$

Where α_l is the liquid phase volume fraction, ρ_l is the liquid density in kg/m^3, T_l is the liquid working fluid temperature in Kelvin, T_{sat} is the working fluid phase change temperature in Kelvin, and S_M is the mass source term.

For the gas phase:

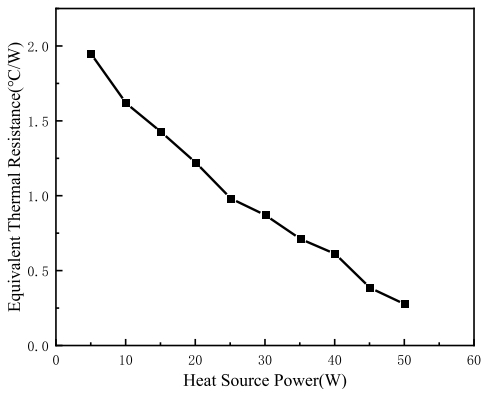

Fig. 5. Equivalent thermal resistance of flat heat pipe.

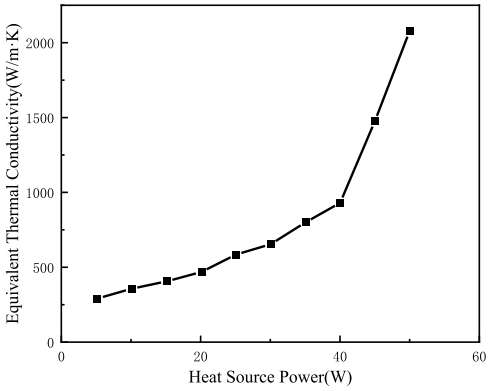

Fig. 6. Equivalent heat transfer coefficient of flat heat pipe.

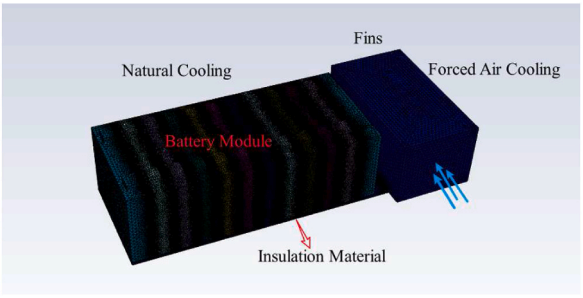

Fig. 7. The grid partitioning of the battery thermal management system.

$$S_M = 0.1\alpha_l\rho_l\left|\frac{T_l - T_{sat}}{T_{sat}}\right| \tag{16}$$

When the condensation $T_v < T_{sat}$ for the liquid phase:

$$S_M = 0.1\alpha_v\rho_v\left|\frac{T_v - T_{sat}}{T_{sat}}\right| \tag{17}$$

Where α_v is the gas phase volume fraction, ρ_v is the gas density in kg/m^3, and T_v is the gas working fluid temperature in Kelvin.

For the gas phase:

$$S_M = -0.1\alpha_v\rho_v\left|\frac{T_v - T_{sat}}{T_{sat}}\right| \tag{18}$$

(2) Energy source term:

Evaporation:

$$S_E = -0.1\alpha_l\rho_l\left|\frac{T_l - T_{sat}}{T_{sat}}\right|\Delta H \tag{19}$$

Where ΔH is the enthalpy of vaporization of the working fluid in kJ/kg, and S_E is the energy source term.

Condensation:

$$S_E = 0.1\alpha_v\rho_v\left|\frac{T_v - T_{sat}}{T_{sat}}\right|\Delta H \tag{20}$$

The user-defined functions written based on the above expressions are loaded into each phase during simulation."

3.2.3. *The overall governing equations*

The general equations consist of unsteady terms, convective terms, heat transfer terms, and source terms.The energy conservation

equation and conductive elements of lithium-ion batteries are as follows [38]:

$$\rho C\frac{\partial T}{\partial t}=\nabla(k\nabla T)+q_v \tag{21}$$

Where C is the specific heat capacity, k is the thermal conductivity, and q_v is the volumetric heat source.

The governing equations for air-cooling are as follows [39]:

$$\rho_a\frac{\partial T_a}{\partial t}+\nabla(\rho_a\vec{v}T_a)=\nabla\left(\frac{k_a}{c_a}\nabla T_a\right) \tag{22}$$

$$\rho_a\frac{d\vec{v}}{dt}=-\nabla p+\mu\nabla^2\vec{v} \tag{23}$$

Where ρ_a , T_a , k_a , and c_a represent air density, temperature, effective thermal conductivity, and specific heat capacity respectively; $\vec{v}$ is the velocity of the air; p and μ are the static pressure and dynamic viscosity of the air.

3.2.4. *Bionic model design parameters*

In the optimization of fluid cooling in industrial manufacturing, inspiration is often drawn from structures found in nature to develop relevant biomimetic designs, as shown in Fig. 8 [40]. Fins inspired by fish scales enhance heat exchange efficiency by increasing surface area, promoting turbulence, and extending the heat exchange pathway. These biomimetic designs can generate favorable thermal performance optimization while considering the practical possibilities of industrial manufacturing applications. By analyzing the erosion patterns of fluids on mechanical surfaces and the structural principles of fish scale surfaces, a biomimetic fish scale structure with protrusions was established, as depicted in Fig. 9. The shape of the protruded surface approximates an ellipse. Considering the characteristics of erosion patterns, the lowest point of the semi-circular protrusion is shifted backward by 1/2R to constitute the biomimetic streamlined structure proposed in this paper, where key structural parameters include R, D, and H. Air fluid should enter from the blunt end of the protrusions of the fish scale biomimetic structure to ensure the effectiveness of the optimized structure. H is calculated according to the formula below based on laminar boundary layer conditions.

$$H=\frac{x}{\sqrt{Re_x}} \tag{24}$$

$$Re_x=\frac{\rho vx}{\mu} \tag{25}$$

In the equation, H represents the boundary layer thickness, x denotes the displacement in the fluid direction, Re_x is the corresponding Reynolds number at position x, v stands for the average fluid velocity, and μ represents the dynamic viscosity of the fluid.The dynamic viscosity of air was set at 1.81×10^{-5} Pa s, and the haracteristic length was selected as 0.08 m. This configuration yielded a Reynolds number of 5420. Given the focus on the flow near the fins, the k-omega model was chosen to analyze the fluid dynamics.

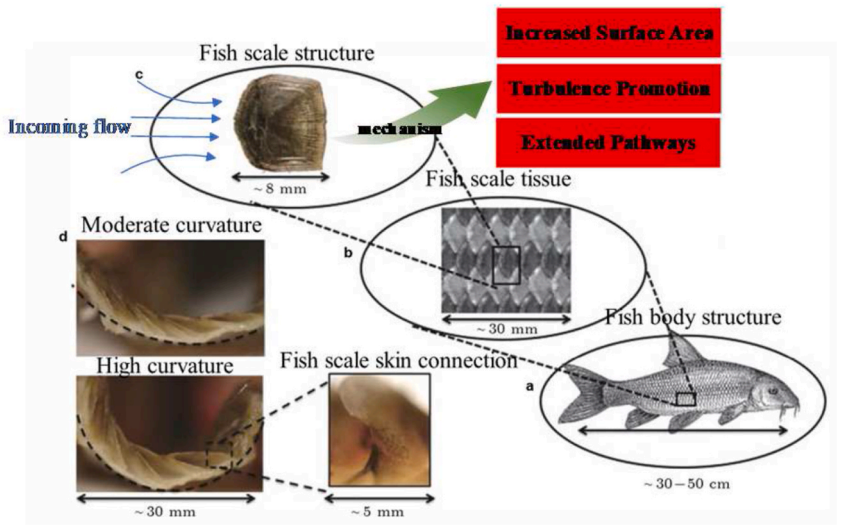

Fig. 8. Fish scale structure.

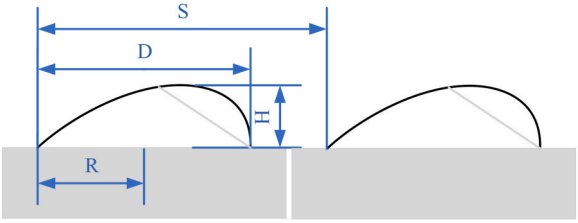

Fig. 9. Biomimetic structure related parameters.

3.2.5. Initial and boundary condition

Before simulation, the initial temperature of the entire system was set to ambient temperature (25 °C). The boundary conditions at the inlet of the air domain were defined with an inlet temperature of 25 °C and an inlet velocity magnitude of 0.1 m/s. The outlet of the channel was set as a pressure outlet with a gauge pressure of 0 Pa. The aluminum plate, heat pipe, and thermal pad between the battery and them were defined as coupled surfaces. Considering the heat transfer during the actual operation of the battery, the third type of boundary condition (i.e., convective heat transfer boundary condition) was applied to solve the equations. Therefore, it was necessary to determine the heat transfer coefficients of the battery's various surfaces and the ambient temperature. Except for the bottom in contact with the thermal pad and the front in contact with the aluminum plate, the remaining surfaces were exposed to natural convection with air, dissipating heat. Hence, the heat transfer coefficients on the battery surfaces were calculated using the following formula:

$$h_a = \frac{Nu\lambda_a}{l} = 0.664\left(\frac{\rho_a v_a l}{\mu_a}\right)^{\frac{1}{2}}\left(\frac{\mu_a C_p}{\lambda_a}\right)^{\frac{1}{3}}\frac{\lambda_a}{l} \tag{26}$$

In the equation, Nu represents the Nusselt number; v_a denotes the velocity of the cooling fluid in meters per second (m/s); ρ_a stands for the density of the gas in kilograms per cubic meter (kg/m^3); μ_a represents the dynamic viscosity of the cooling gas in Pascal-seconds (Pa·s); λ_a signifies the thermal conductivity of the cooling gas in watts per meter-kelvin (W/m·K); C_p represents the specific heat capacity of the cooling gas in joules per kilogram-kelvin (J/kg·K); and l denotes the characteristic length of the heat transfer surface in meters(m). The surface natural convection heat transfer coefficient was calculated to be 8.32 W/m^2·K.

A no-slip boundary condition was applied at the interface between the fluid channel and the heat dissipation fins. A layer of insulation material was installed at the bottom of the thermal management system and set as an adiabatic wall condition.

3.2.6. Grid independence

Fig. 7 depicts the application of a hexahedral mesh in the computational domain of the BTMS model based on FHP. The initial boundaries were set according to the operating conditions described in the previous section. To ensure the accuracy of the numerical simulation results, an independence test was conducted on the computational domain mesh, and the results are presented in Fig. 10. As the number of grid cells increased from 320,000 to 480,000, the maximum temperature deviation of the battery remained below 1 %. Therefore, a grid with 320,000 cells was selected for the numerical simulation.

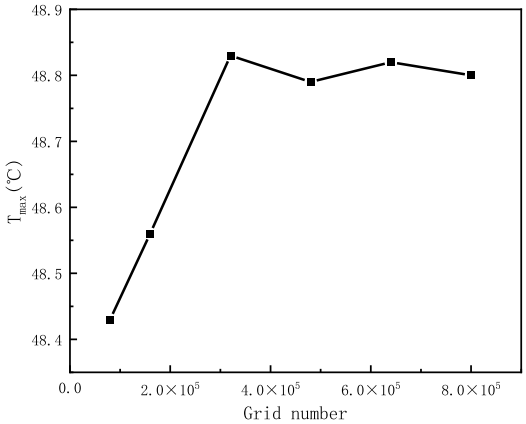

Fig. 10. Grid independence analysis.

4. Experimental validation

4.1. Heat pipe verification

In order to verify the accuracy of the flat plate heat management theoretical model, testing was conducted on the temperature distribution of the heat pipe under various operating conditions. The testing cross-section is depicted in Fig. 11. The experimental setup comprised a heat pipe, heat sinks, a direct current power supply (KANGKESI), a data acquisition instrument (TOPRIE TP9000), and a cooling fan. Throughout the experimental procedure, a constant heat flux was transferred to the evaporator section of the heat pipe from the direct current power supply via a uniform heat source. Air at 25 °C circulated through the heat sinks of the condenser section, and several K-type thermocouples (with an accuracy of ±0.5 °C) were arranged on the surface of the heat pipe for temperature measurements. Fig. 12 illustrates the temperature distribution of the heat pipe under different operating conditions and compares the numerical simulation results. It is evident from the figure that the maximum relative errors between experimental and simulated results are 5.6 % and 4.4 % for heat generation rates of 15 W and 20 W, respectively. The notable consistency in temperature distribution between numerical simulations and experiments indicates a good agreement between the theoretical model of the heat pipe and actual observations.

4.2. Battery thermal management system verification

Fig. 13 depicts the schematic diagram of the temperature sensor arrangement within the battery pack. The final assessment of the battery pack's temperature is derived by averaging the readings from sensors on three strategically positioned batteries—at the front, middle, and rear. This calculated average reflects the comprehensive thermal state of the entire battery pack. To ensure the accuracy of the simulations, the experimental setup depicted in Figs. 14 and 15 was employed to validate the Flat Heat Pipe-based Battery Thermal Management System (BTMS) model. This setup included battery testing equipment, a constant temperature and humidity chamber, data acquisition instruments, a control computer, a prismatic battery array, and a flat heat pipe with fins at the condensation section. The battery cells were sequentially numbered from 01 to 12 from left to right in accordance with the direction of vapor flow. Thermal grease was applied between the battery module and the evaporation section of the flat heat pipe to reduce contact thermal resistance. Additionally, an insulated mat was installed beneath the flat heat pipe to prevent heat transfer to the ground. Air cooling was facilitated by a fan and air channel at the condensation section, with the air velocity measured by an anemometer. The BTMS operated under natural convection conditions, with the ambient temperature maintained at approximately 25 °C. The module was allowed to cool in the environment for over 8 h before initiating the subsequent discharge process. The battery testing instrument (CTE-8000) was utilized for real-time monitoring and recording of battery current, voltage, and other relevant data, exhibiting a relative measurement error of less than 0.1 %. The constant temperature and humidity chamber (SY-303) was used to maintain precise environmental temperatures, with an error margin of less than 0.5 °C. The data acquisition system, coupled with K-type thermocouples (Model WRNT-01-2PBO, with a temperature measurement range of 0–600 °C), was utilized to record surface temperatures and estimate the average temperature of the battery. Temperature data was captured at a rate of one sample per second. In this experiment, temperature was the primary source of uncertainty, stemming from measurement errors associated with the instruments used. Initially, the error in temperature primarily originated from the thermocouples and data acquisition system. The K-type thermocouples employed in this study had an accuracy of ±0.4 %. The temperature data collected using a data acquisition system with an accuracy of ±0.1 % were analyzed to calculate the standard deviation of measurement error, σ_D, found to be 3.3 %. Consequently, the total error, σ, was calculated using the following formula to be 0.412 %.

$$\sigma = \pm\sqrt{(\sigma_T^2 + \sigma_D^2)}$$

Thermal pads were utilized to fill gaps between components to reduce thermal resistance. Furthermore, the system's exterior was

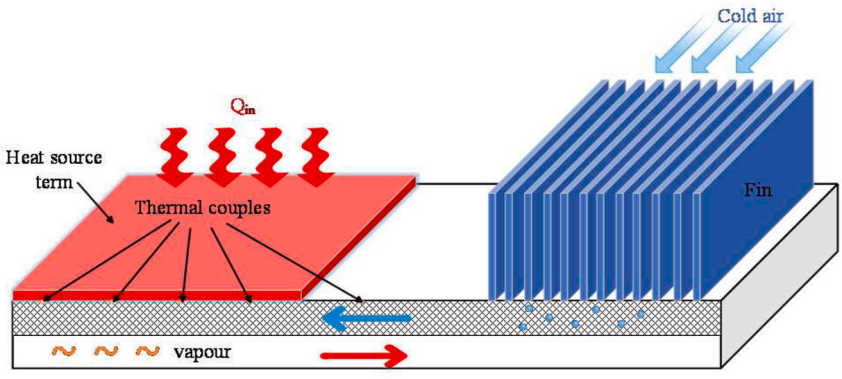

Fig. 11. The cross-section of the test system.

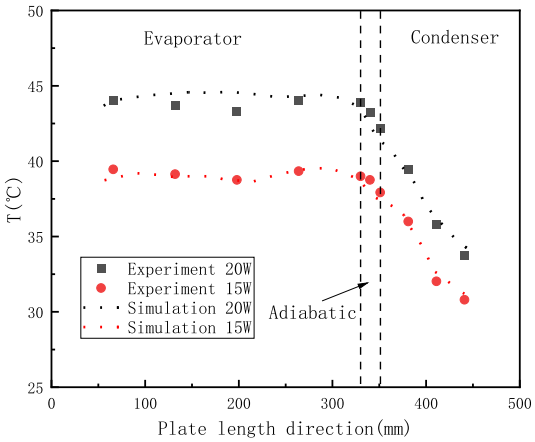

Fig. 12. The temperature distribution of the heat pipe.

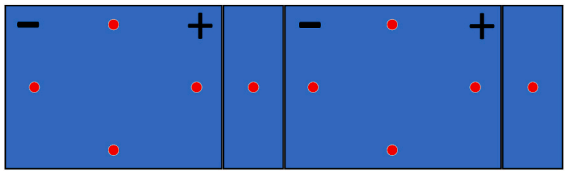

Fig. 13. Temperature sensor layout diagram.

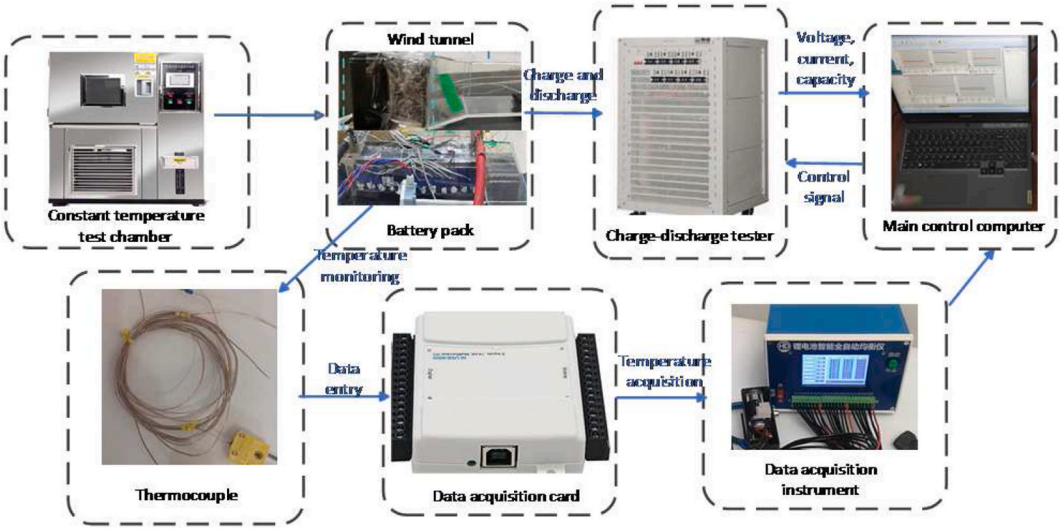

Fig. 14. Schematic diagram of experimental device based on flat heat pipe.

covered with insulating material to minimize heat exchange with the surroundings.

The experimental comparison between battery surface temperature variations and simulations is depicted in Fig. 16. Discharge rates of 1 C and 3 C were applied, with the abscissa indicating the depth of discharge (DOD), which refers to the ratio of the discharged capacity to the total capacity of the battery. In other words, it denotes the proportion of available capacity that the battery has discharged. It can be readily observed from the figure that, towards the end of discharge, the errors between experimental and simulated temperatures are less than 1.8 % and 4.5 %, respectively. This outcome suggests that the simulation model established in this study effectively represents the actual temperature variations.

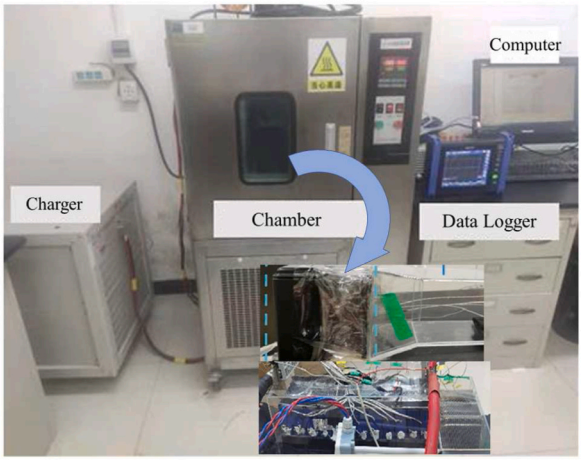

Fig. 15. Overall experimental setup diagram.

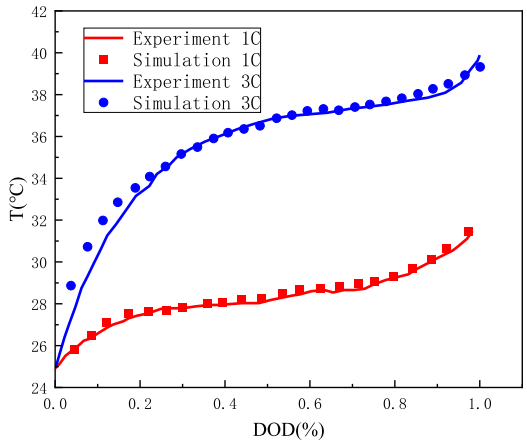

Fig. 16. The variation of battery surface temperature.

5. Results and discussions

5.1. Orthogonal experiment analysis

As mentioned earlier, the main factors influencing the temperature distribution of battery modules include four factors. In order to obtain balanced samples for multiple influencing factors and reduce the time cost of experiments, an orthogonal experimental method was employed in this study. The orthogonal experimental method can effectively obtain balanced samples for multiple factors by selecting representative cases, while also reducing the number of tests in the experiment. The computational domain of the battery module includes 12 battery cells and an aluminum plate sandwiched between them. The factors investigated include protrusion diameter (D), protrusion height (H), protrusion spacing (S), and fin height (L). A four-level orthogonal experiment was conducted for these four factors, with the maximum temperature and temperature difference of the battery being used as performance evaluation indicators. The orthogonal experimental table for the four factors and four levels is shown in Table 4.

Table 4
Four-factor level.

Level	Factors			
	D(mm)	H(mm)	S(mm)	L(mm)
1	10	1.75	7	75
2	12.5	2.5	9	80
3	15	3.25	11	85
4	17.5	4	13	90

Table 5
Parameter setting and results of 16 orthogonal experiments.

Case	Factors				Indicators	
	D(mm)	H(mm)	S(mm)	L(mm)	T_{max} (°C)	ΔT (°C)
1	10	1.75	7	75	42.05	6.18
2	10	2.5	9	80	40.08	5.01
3	10	3.25	11	85	38.77	4.13
4	10	4	13	90	37.78	3.39
5	12.5	1.75	9	85	39.67	4.66
6	12.5	2.5	7	90	40.21	5.68
7	12.5	3.25	13	75	37.89	3.01
8	12.5	4	11	80	38.20	3.71
9	15	1.75	11	90	38.17	3.57
10	15	2.5	13	85	37.24	2.79
11	15	3.25	7	80	39.73	5.31
12	15	4	9	75	38.77	4.25
13	17.5	1.75	13	80	37.48	2.78
14	17.5	2.5	11	75	37.96	3.23
15	17.5	3.25	9	90	38.08	4.07
16	17.5	4	7	85	39.08	5.10

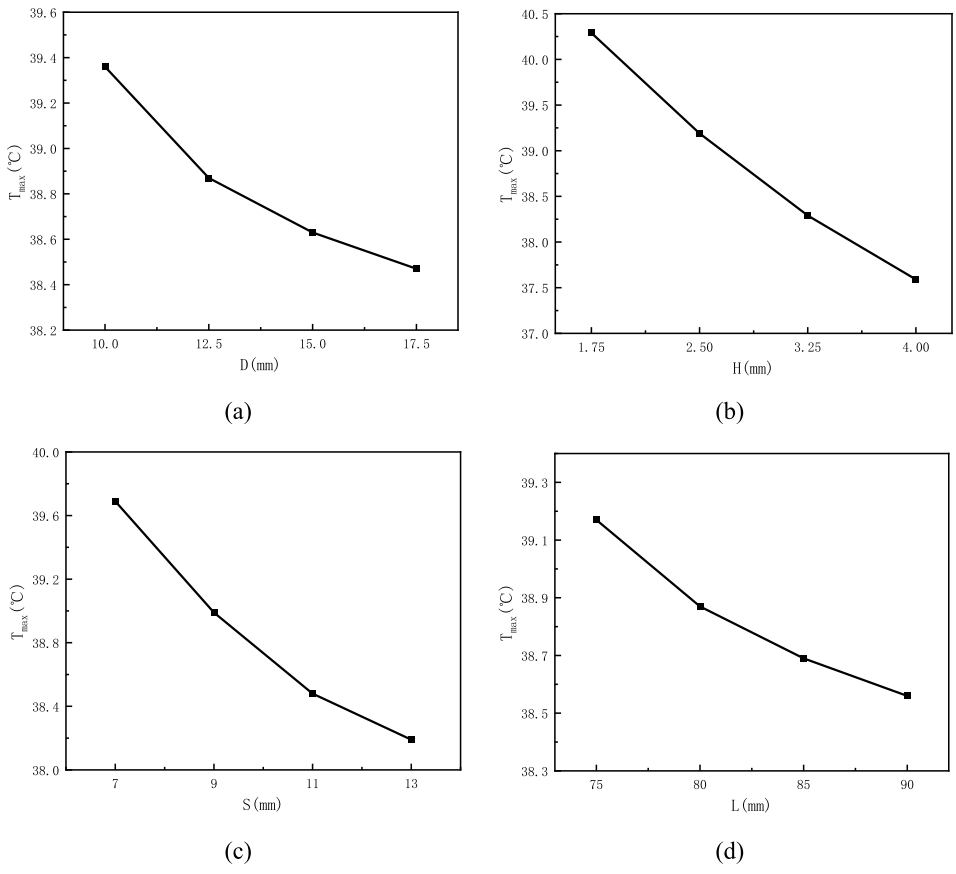

Fig. 17. The impact of factors at different levels on the maximum temperature.

The detailed arrangement of the orthogonal experiments is presented in Table 5. In each scenario, the battery was discharged at 3 C. Table 5 also provides the results of the orthogonal experimental designs. According to the survey results, the maximum temperatures of Scenarios 1, 2, and 5 exceeded 40 °C, while those of Scenarios 5, 11, and 16 approached 40 °C. Additionally, the maximum temperature differences of Cases 1, 2, 6, 11, and 16 exceeded 5 °C, indicating that these cases failed to meet thermal management requirements. Thus, to ensure the proper operating conditions of the battery, appropriate values for each influencing factor must be selected. To determine the suitable range for each factor, the average values of indicators at different levels were calculated and analyzed. Fig. 17

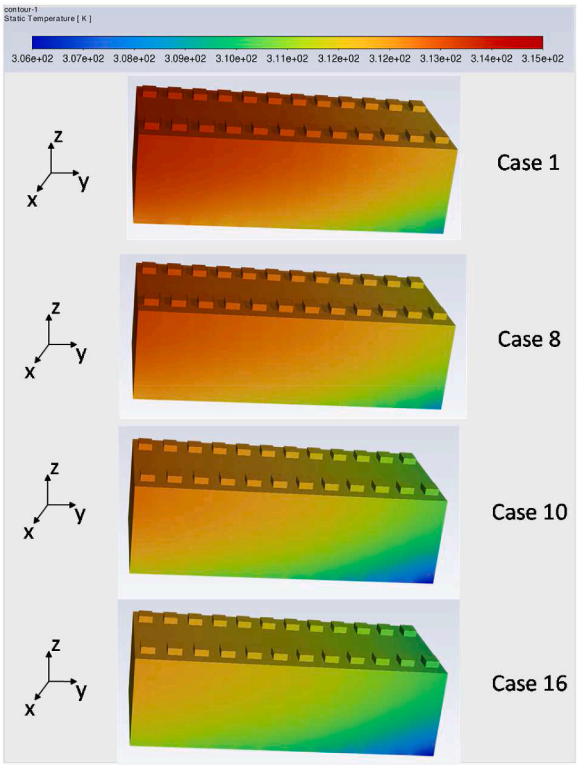

Fig. 18. The distribution of battery temperatures under various operating conditions.

illustrates the variation of the maximum temperature with different levels of each factor. The results indicate that as the value of each factor increases, the battery's maximum temperature decreases. This is because increasing the values of D, S, and L increases the contact area between components and the fluid, thereby enhancing heat dissipation. When the value of H increases, it not only increases the heat transfer area of the fluid but also generates local turbulence, enhancing the heat transfer coefficient, reducing thermal resistance, improving heat transfer efficiency, and consequently lowering Tmax. It is recommended to set 40 °C as the upper limit for Tmax, with values of D, H, S, and L being greater than 12.5 mm, 3.25 mm, 9 mm, and 80 mm, respectively. Fig. 18 illustrates the temperature distribution of some numerical cases.

The maximum temperature of the battery module is influenced by the total thermal resistance of the overall cooling system, while the temperature difference is primarily caused by the non-uniformity of the thermal conductivity of the battery in three-dimensional space. The variation of temperature difference with different levels of each factor is depicted in Fig. 19. Changes in S and L significantly affect temperature uniformity. When the values of S and L increase from Level 1 to Level 4, the temperature difference decreases by approximately 0.92 °C and 2.55 °C, respectively. However, the impact of D and H on temperature uniformity is relatively minor. Therefore, further investigation is necessary to analyze the sensitivity of these influencing factors to the maximum temperature and temperature difference. In general, larger values of these influencing factors reduce the system's thermal resistance and lead to improved cooling performance of the system.

5.2. Parameter sensitivity evaluation

The maximum temperature and temperature uniformity of the battery module are influenced by four key factors. These factors were systematically evaluated using orthogonal experiments to ensure a comprehensive understanding of their individual and combined effects.To assess the correlation between these factors and the targeted indicators, the study employed the fuzzy grey relational analysis method. By integrating the results of the orthogonal experiments with the fuzzy grey relational analysis, the study provided a robust framework for optimizing the thermal management system in battery modules.

5.2.1. Analysis of the maximum temperature

The maximum temperature is a critical parameter for assessing the operational performance and safety of battery packs. Based on

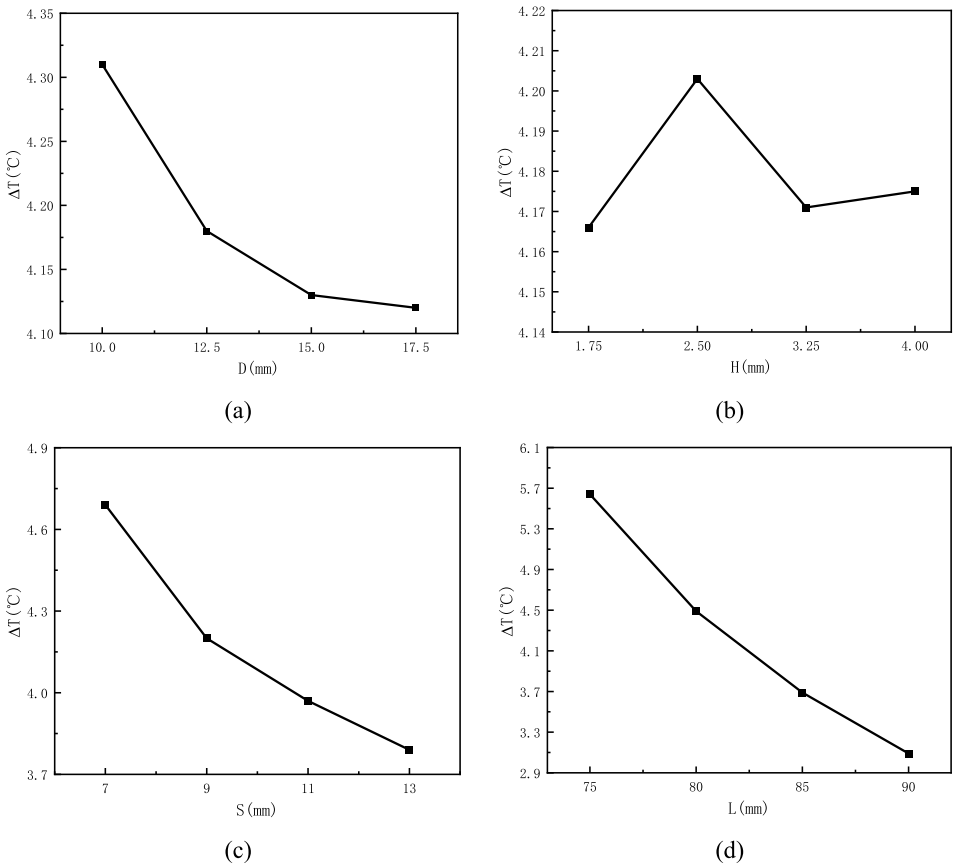

Fig. 19. The influence of factors at different levels on the maximum temperature difference.

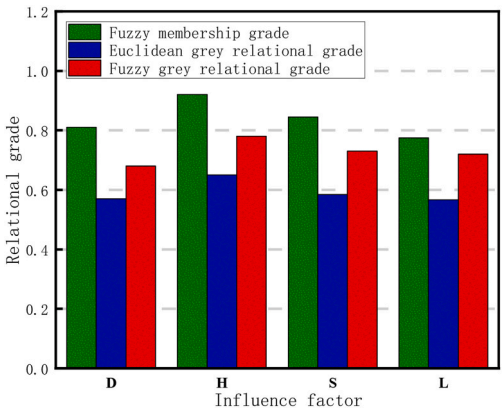

Fig. 20. Fuzzy correlation analysis on maximum temperature.

16 computational cases, the four influencing factors, D, H, S, and L, are respectively considered as comparison arrays x_1, x_2, x_3, and x_4. Meanwhile, Tmax is established as the reference array Y_1. The comparison and reference arrays can be expressed as follows:

$$X=\begin{bmatrix} x_1 \\ x_2 \\ x_3 \\ x_4 \end{bmatrix}=\begin{bmatrix} 10 & 10 & 10 & 10 & 12.5 & 12.5 & 12.5 & 12.5 & 15 & 15 & 15 & 15 & 17.5 & 17.5 & 17.5 & 17.5 \\ 1.75 & 2.5 & 3.25 & 4 & 1.75 & 2.5 & 3.25 & 4 & 1.75 & 2.5 & 3.25 & 4 & 1.75 & 2.5 & 3.25 & 4 \\ 7 & 9 & 11 & 13 & 9 & 7 & 13 & 11 & 11 & 13 & 7 & 9 & 13 & 11 & 9 & 7 \\ 75 & 80 & 85 & 90 & 85 & 90 & 75 & 80 & 90 & 85 & 80 & 75 & 80 & 75 & 90 & 85 \end{bmatrix}$$

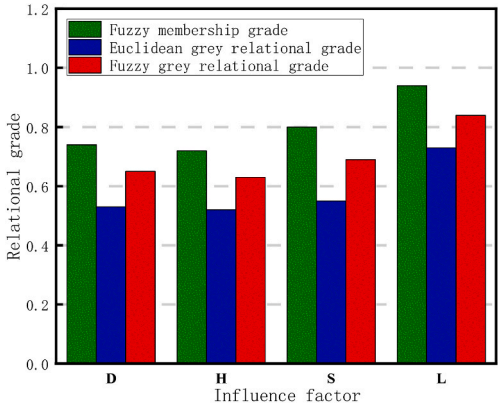

Fig. 21. Fuzzy correlation analysis on the maximum temperature difference.

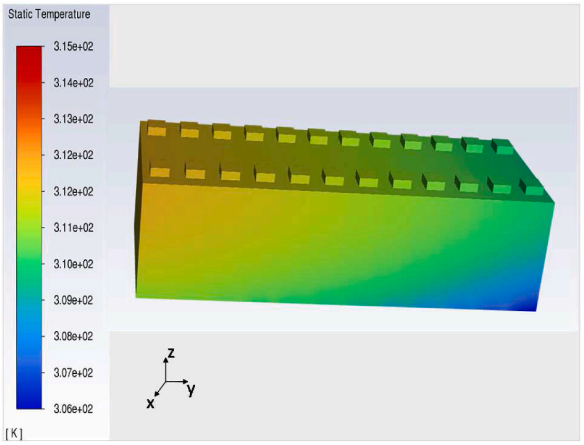

Fig. 22. Temperature distribution under optimal parameters.

$$Y_1 = [42.05 \;\; 40.08 \;\; 38.77 \;\; 37.78 \;\; 39.67 \;\; 40.21 \;\; 37.89 \;\; 38.20 \;\; 38.17 \;\; 37.24 \;\; 39.73 \;\; 38.77 \;\; 37.48 \;\; 37.96 \;\; 38.08 \;\; 39.08]$$

As the objective of thermal management strategies is to reduce the maximum temperature of the battery pack, it is necessary to normalize and dimensionless Y_1 to accurately demonstrate its correlation with temperature reduction. Therefore, the expression for dimensionless treatment of Y_1 is as follows:

$$Y_1(k)' = \frac{y_1(k) - max\, y_j(k)}{min\, y_j(k) - max\, y_j(k)} \tag{27}$$

Through equation (4), dimensionless treatment can be applied to the comparison array for comparison. After dimensionless treatment, the matrices of the comparison and reference arrays are as follows:

$$X = \begin{bmatrix} x_1 \\ x_2 \\ x_3 \\ x_4 \end{bmatrix} = \begin{bmatrix} 0 & 0 & 0 & 0 & 0.33 & 0.33 & 0.33 & 0.33 & 0.67 & 0.67 & 0.67 & 0.67 & 1 & 1 & 1 & 1 \\ 0 & 0.33 & 0.67 & 1 & 0 & 0.33 & 0.67 & 1 & 0 & 0.33 & 0.67 & 1 & 0 & 0.33 & 0.67 & 1 \\ 0 & 0.33 & 0.67 & 1 & 0.33 & 0 & 1 & 0.67 & 0.67 & 1 & 0 & 0.33 & 1 & 0.67 & 0.33 & 0 \\ 0 & 0.33 & 0.67 & 1 & 0.67 & 1 & 0 & 0.33 & 1 & 0.67 & 0.33 & 0 & 0.33 & 0 & 1 & 0.67 \end{bmatrix}$$

$$Y_1 = [0 \;\; 0.41 \;\; 0.68 \;\; 0.89 \;\; 0.49 \;\; 0.38 \;\; 0.86 \;\; 0.80 \;\; 0.81 \;\; 1 \;\; 0.48 \;\; 0.68 \;\; 0.95 \;\; 0.85 \;\; 0.83 \;\; 0.62]$$

Based on the matrices, the cosine values of fuzzy membership degrees and Euclidean grey relational degrees are calculated using equations (5)–(9). These metrics assess the similarity and distance between factors and indicators. The results show that factor H has the highest values, while factor L has the lowest. The fuzzy grey relational degree is then computed using equation (10). For maximum temperature, the fuzzy grey relational degrees for the four factors, S, D, H, and L, are 0.7312, 0.6898, 0.7871, and 0.6697, respectively, as shown in Fig. 20. This indicates that the primary factor influencing the maximum temperature of the battery module is H, followed

by S and D, with L having the least impact.

5.2.2. Analysis of the maximum temperature difference

Temperature difference is an important parameter for evaluating the uniformity of battery modules, significantly impacting the operational performance of batteries. In this section, the influence of four factors on temperature difference will be investigated, with T being designated as the reference array Y_2, expressed as follows:

$$Y_2 = [6.18 \quad 5.01 \quad 4.13 \quad 3.39 \quad 4.66 \quad 5.68 \quad 3.01 \quad 3.71 \quad 3.57 \quad 2.79 \quad 5.31 \quad 4.25 \quad 2.78 \quad 3.23 \quad 4.07 \quad 5.10]$$

The dimensionless treatment of Y2 is calculated using equation (4). The fuzzy membership degrees and Euclidean grey relational degrees of temperature difference are computed using equations (5)–(9), based on the comparison arrays x_1, x_2, x_3, x_4, and the reference array Y_2.Fig. 21 illustrates the fuzzy membership degrees and Euclidean grey relational degrees for the four factors on temperature difference. L ranks first in both fuzzy membership degrees and Euclidean grey relational degrees, indicating a significant correlation with temperature difference. The values of D and H are relatively small, suggesting their relative independence from temperature difference. The fuzzy grey relational degrees of the four influencing factors are calculated through equation (10), yielding values of 0.6798, 0.6356, 0.8494, and 0.6182 (as shown in Fig. 21). The structural parameters of L significantly impact the temperature uniformity of battery modules. The ranking of factors influencing temperature uniformity is as follows: L, S, D, and H.

The structural parameters of fins are crucial for the cooling performance of the system. The height (H) of protrusions has the most significant impact on the distribution of maximum temperature in the battery module. The fin height (L) greatly influences the temperature uniformity of the battery pack. The optimal settings for multiple parameters are: D = 17.5 mm, H = 4 mm, S = 13 mm, and L = 90 mm. In the optimal scenario, the maximum temperature of the battery module is 36.52 °C, with a temperature difference of 2.65 °C. The temperature distribution of the optimal scenario is depicted in Fig. 22. The optimal model demonstrates superior cooling performance compared to other scenarios.

6. Conclusions

This paper explores the cooling efficacy of a battery thermal management system, specifically examining the thermal behavior of a flat heat pipe. Orthogonal design experiments coupled with fuzzy grey relational analysis were utilized to assess four structural parameters of the aluminum plate: height, thickness, and angles of coverage relative to the battery and the heat pipe. This study identified the key influencing factors and their optimal configurations.

The results indicate that to keep the battery temperature below 40 °C, the dimensions of the heat pipe's diameter, height, the spacing between protrusions, and the height of the heat sink fins should be a minimum of 12.5 mm, 3.25 mm, 9 mm, and 80 mm, respectively. The fuzzy grey relational analysis demonstrated varying impacts of these parameters on the maximum temperature and temperature disparity across the system.

Optimal parameter values were established as follows: protrusion diameter of 17.5 mm, height of 4 mm, spacing of 13 mm, and heat sink fin height of 90 mm. Under these conditions, the maximum temperature recorded for the battery module was 36.52 °C, with a temperature differential of 2.65 °C. These findings offer critical insights into refining the design of battery thermal management systems to enhance cooling performance and maintain safe operational temperatures.

Data availability

Data will be made available on request.

CRediT authorship contribution statement

Zeyu Liu: Writing – review & editing, Writing – original draft, Methodology. **Chengfeng Xiong:** Visualization, Validation, Investigation, Formal analysis, Data curation. **Xiaofang Du:** Software, Project administration, Funding acquisition, Data curation, Conceptualization.

Declaration of competing interest

The authors declare that they have no known competing financial interests or personal relationships that could have appeared to influence the work reported in this paper.

Acknowledgements

The authors greatly appreciate the equipment and financial support from the Hubei Key Laboratory.

References

[1] Z. Guo, et al., Battery thermal management system with heat pipe considering battery aging effect, Energy 263 (2023) 126116, https://doi.org/10.1016/j.energy.2022.126116.

[2] I. Jarraya, F. Abdelhedi, N. Rizoug, An innovative power management strategy for hybrid battery–supercapacitor systems in electric vehicle, Mathematics 12 (1) (2023) 50, https://doi.org/10.3390/math12010050.
[3] H. Liu, et al., A parametric study of a hybrid battery thermal management system that couples PCM/copper foam composite with helical liquid channel cooling, Energy 231 (2021) 120869, https://doi.org/10.1016/j.energy.2021.120869.
[4] Z. Wei, Z. Jiangbin, C. Rathberger, Using latent heat storage for improving battery electric vehicle thermal management system efficiency, SAE Int. J. Elec. Veh. 13 (2) (2024) 231–247, https://doi.org/10.4271/14-13-02-0012.
[5] H.C. Graichen, et al., The impact of a combined battery thermal management and safety system utilizing polymer mini-channel cold plates on the thermal runaway and its propagation, Batteries 10 (1) (2023) 1, https://doi.org/10.3390/batteries10010001.
[6] B. Deng, et al., Improving a fuel cell system's thermal management by optimizing thermal control with the particle swarm optimization algorithm and an artificial neural network, Appl. Sci. 13 (23) (2023) 12895, https://doi.org/10.3390/app132312895.
[7] V. Lucaferri, et al., A review on battery model-based and data-driven methods for battery management systems, Energies 16 (23) (2023) 7807, https://doi.org/10.3390/en16237807.
[8] Z. Xia, et al., Experimental study of a passive thermal management system using expanded graphite/polyethylene glycol composite for lithium-ion batteries, Energies 16 (23) (2023) 7786, https://doi.org/10.3390/en16237786.
[9] P. Fu, et al., A review of cooling technologies in lithium-ion power battery thermal management systems for new energy vehicles, Processes 11 (12) (2023) 3450, https://doi.org/10.3390/pr11123450.
[10] D. Arora, A. El-Sharkawy, S. Panchal, Development of time-temperature analysis algorithm for estimation of lithium-ion battery useful life, SAE Technical Paper (2024) 12, https://doi.org/10.4271/2024-01-2191.
[11] A.M. Fathoni, N. Putra, T.M.I. Mahlia, A systematic review of battery thermal management systems based on heat pipes, J. Energy Storage 73 (2023) 109081, https://doi.org/10.1016/j.est.2023.109081.
[12] Y.M. Alkhulaifi, N.A.A. Qasem, S.M. Zubair, Exergoeconomic assessment of the ejector-based battery thermal management system for electric and hybrid-electric vehicles, Energy 245 (2022) 123252, https://doi.org/10.1016/j.energy.2022.123252.
[13] P.K. Koorata, et al., Investigation of the thermal performance of biomimetic minichannel-based liquid-cooled large format pouch battery pack, J. Energy Storage 84 (2024) 110928, https://doi.org/10.1016/j.est.2024.110928.
[14] J. Pu, et al., Structural Optimization of a Serpentine-Channel Cold Plate for Thermal Management of Lithium-Ion Battery Based on the Field Synergy Principle, 2024, https://doi.org/10.2139/ssrn.4795285. Available at: SSRN 4795285.
[15] H. Chen, et al., Steady and transient sensitivity investigations on a passive battery thermal management system coupling with phase change materials and heat pipes: full numerical modeling and orthogonal tests, J. Energy Storage 73 (2023) 109054, https://doi.org/10.1016/j.est.2023.109054.
[16] X. Zhang, et al., A review on thermal management of lithium-ion batteries for electric vehicles, Energy 238 (2022) 121652, https://doi.org/10.1016/j.energy.2021.121652.
[17] H. Shi, et al., Multi-objective optimization of integrated lithium-ion battery thermal management system, Appl. Therm. Eng. 223 (2023) 119991, https://doi.org/10.1016/j.applthermaleng.2023.119991.
[18] V. Talele, et al., Improving battery safety by utilizing composite phase change material to delay the occurrence of thermal runaway event, Int. Commun. Heat Mass Tran. 155 (2024) 107527, https://doi.org/10.1016/j.icheatmasstransfer.2024.107527.
[19] A.H. Vakilzadeh, et al., Heat transfer and fluid flow in a PCM-filled enclosure: effect of heated wall configuration, J. Energy Storage 87 (2024) 111448, https://doi.org/10.1016/j.est.2024.111448.
[20] L. He, et al., Review of thermal management system for battery electric vehicle, J. Energy Storage 59 (2023) 106443, https://doi.org/10.1016/j.est.2022.106443.
[21] M. Zheng, et al., Numerical study on power battery thermal management system based on heat pipe technology, Energy Rep. 9 (2023) 350–361, https://doi.org/10.1016/j.egyr.2022.11.187.
[22] Y. Wang, et al., A coupled model and thermo-electrical performance analysis for flat heat pipe-based battery thermal management system, Appl. Therm. Eng. 233 (2023) 121116, https://doi.org/10.1016/j.applthermaleng.2023.121116.
[23] R. Ren, et al., Experimental study on top liquid-cooling thermal management system based on Z-shaped micro heat pipe array, Energy 282 (2023) 128321, https://doi.org/10.1016/j.energy.2023.128321.
[24] C. Wu, et al., A new design of cooling plate for liquid-cooled battery thermal management system with variable heat transfer path, Appl. Therm. Eng. 239 (2024) 122107, https://doi.org/10.1016/j.applthermaleng.2023.122107.
[25] X. Chen, et al., Performance of thermal management system for cylindrical battery containing bionic spiral fin wrapped with phase change material and embedded in liquid cooling plate, Renew. Energy 223 (2024) 120087, https://doi.org/10.1016/j.renene.2024.120087.
[26] J. Xie, et al., A novel strategy to optimize the liquid cooling plates for battery thermal management by precisely tailoring the internal structure of the flow channels, Int. J. Therm. Sci. 184 (2023) 107877, https://doi.org/10.1016/j.ijthermalsci.2022.107877.
[27] F. Zhang, et al., Structural optimization of thermal management system for bionic liquid cold battery based on fuzzy grey correlation analysis, Appl. Therm. Eng. 249 (2024) 123347, https://doi.org/10.1016/j.applthermaleng.2024.123347.
[28] W. Xu, et al., Crushing responses and energy absorption of bionic inspired corrugated honeycombs, Int. J. Impact Eng. 179 (2023) 104641, https://doi.org/10.1016/j.ijimpeng.2023.104641.
[29] X. Xiong, et al., Numerical analysis of cylindrical lithium-ion battery thermal management system based on bionic flow channel structure, Therm. Sci. Eng. Prog. 42 (2023) 101879, https://doi.org/10.1016/j.tsep.2023.101879.
[30] A. Tang, et al., Orthogonal design based pulse preheating strategy for cold lithium-ion batteries, Appl. Energy 355 (2024) 122277, https://doi.org/10.1016/j.apenergy.2023.122277.
[31] Y. Kuo, T. Yang, G.W. Huang, The use of grey relational analysis in solving multiple attribute decision-making problems, Comput. Ind. Eng. 55 (1) (2008) 80–93, https://doi.org/10.1016/j.cie.2007.12.002.
[32] Y. Sun, S. Liu, L. Li, Grey correlation analysis of transportation carbon emissions under the background of carbon peak and carbon neutrality, Energies 15 (9) (2022) 3064, https://doi.org/10.3390/en15093064.
[33] Xiangjie Li, Design and Optimization of Automotive Power Battery Thermal Management System Based on Flat Heat Pipes, Chongqing University, 2022. https://link.cnki.net/doi/10.27670/d.cnki.gcqdu.2022.003300.
[34] M. Zheng, et al., Numerical study on power battery thermal management system based on heat pipe technology, Energy Rep. 9 (2023) 350–361, https://doi.org/10.1016/j.egyr.2022.11.187.
[35] X. Wang, et al., Cavity structure-based active controllable thermal switch for battery thermal management, iScience 26 (12) (2023), https://doi.org/10.1016/j.isci.2023.108419.
[36] J. Zhang, et al., Experimental and numerical investigation on efficient optimization of battery thermal management systems, Appl. Therm. Eng. 221 (2023) 119821, https://doi.org/10.1016/j.applthermaleng.2022.119821.
[37] Jing Ma, et al., Numerical simulation on the heat dissipation characteristics of lithium battery for energy storage based on heat pipe, Zhongguo Dianji Gongcheng Xuebao/Proceedings of the Chinese Society of Electrical Engineering 43 (17) (2023) 6737–6745, https://doi.org/10.13334/j.0258-8013.pcsee.222840.
[38] Q. Zhang, G. Cao, X. Zhang, Study of wet cooling flat heat pipe for battery thermal management application, Appl. Therm. Eng. 219 (2023) 119407, https://doi.org/10.1016/j.applthermaleng.2022.119407.
[39] O. Yetik, U. Morali, T.H. Karakoc, A numerical study of thermal management of lithium-ion battery with nanofluid, Energy 284 (2023) 129295, https://doi.org/10.1016/j.energy.2023.129295.
[40] Yun Xing, Jialing Yang, Research on the anti-impact strategy and its bionic mechanism of animal evolution, Advances in Mechanics 51 (2) (2021) 295–341, https://doi.org/10.6052/1000-0992-20-027.